Induced drag in two dimensions in ideal fluids

Journal of Physics Communications

PAPER

Induced drag in two dimensions in ideal fluids

R W Meyer[1] and S Erland[2]

[1] Department of mechanical and marine engineering, Western Norway University of Applied Sciences, Haugesund, Norway
[2] Department of maritime studies, Western Norway University of Applied Sciences, Haugesund, Norway

E-mail: runald.meyer@hvl.no

Keywords: drag coefficient, Von Karman vortex street, ideal fluids, induced drag, circulation, potential flow, wing sections

OPEN ACCESS

RECEIVED
20 June 2019

REVISED
3 October 2019

ACCEPTED FOR PUBLICATION
22 October 2019

PUBLISHED
6 November 2019

Abstract

In this paper we suggest a model for how a significant part of the drag forces on two-dimensional objects can be derived using the circulation that is naturally maintained around the objects. We assume incompressible and inviscid potential flow and that the circulation is already generated. The resulting velocity field complements the one that is known to generate Prandtl's induced drag in three dimensions. We demonstrate how fluid particles in a velocity field are attracted towards an object, and that this, due to conservation of momentum, results not only in lift, but also in drag forces. The magnitude of a disturbance velocity can be derived from the circulation of bound and shed vortices accompanying the object and parameters taken from the von Kármán vortex street description. Another part of the drag is generated by vortices that emerge behind blunt bodies when fluid particles do not follow the surface of the objects. We obtain a mathematical description of the resistance of several types of blunt bodies and rotating cylinders. The model involves no parameters that are derived from empirical data. Still, this inviscid approach corresponds well with experimental data in viscous flow and is close to a mathematical empirical description of rotating cylinders by W. G. Bickley.

1. Introduction

The model of perfect or ideal fluids is incapable of explaining many of the observed facts of fluid motion. The paradox of d'Alembert stating that a solid moving through an ideal fluid with constant velocity will not experience resultant forces is in contradiction with the observed facts and makes it difficult to explain the connection between lift and drag. It was the work by Lanchester [1] and Prandtl [2] that showed that a part of the drag of a finite wing in ideal fluids could be explained using the model of a circulation generated by the airfoil. This circulation will need viscosity to originate, which we do not find in the ideal model. However, assuming that the circulation is already produced, the induced drag follows from the theory of ideal fluids.

The main theoretical approach presently used to study external flows, is boundary-layer theory (see e.g. [3]). The design of profiles for subsonic speeds, is usually assisted by computer programs (see e.g. [4, 5]), where the method of conformal mapping or panel methods are applied. Friction is determined by the construction of an integral boundary layer that is based on empirical data. These methods are also taking into account displacement effects and the influence of local bubbles. These approaches take both microscopic and macroscopic effects into account, including viscous effects. We will follow an alternative approach, by looking deeper into the macroscopic effect of the vortices (see e.g. [6]) that are generated by the unsteady flow past an object. Although viscosity is needed to start such a circulation, we assume ideal fluid in the subsequent process.

It is known, that a body moving through a fluid generates a 'train' of eddies. Bickley [7] examined the case of two-dimensional flow past rotating circular cylinders in ideal fluids. He investigated the resulting force on the cylinder by using the full pressure equation and deriving the velocity potential from the stream function. By placing a vortex behind the cylinder that had the opposite circulation as the cylinder, and estimating the position of the outside vortex, he derived formulas for the drag- and lift coefficients. They are determined by the circulation, the velocity of the flow against the cylinder, and a relation between cylinder diameter and distance to

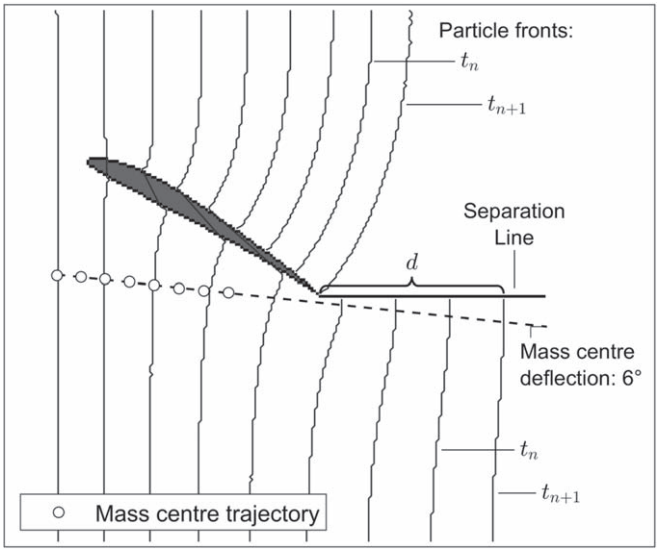

Figure 1. The trajectory of the mass centre of a 'particle cloud', generated using the 'Random Walk Source Model' in [8, 9] as an average over 400 different runs. Particles are coming out of a vertical line source on the left side, generating a front. The front is passing the wing section with 30° angle of attack. The wing section is an obstacle separating the front into two segments, and a separation line keeps the two front segments separated to follow the Kutta condition. The lower front segment at time step t_{n+1} is ahead of the upper segment by a distance d. This distance defines the circulation around the profile (see section 3.2.1). Some positions on the trajectory of the mass centre of the particle cloud are shown as circles. The dashed line indicates the deflection of the mass centre trajectory.

the vortex core. The lift and drag curves Bickley obtained from the equations are all parabolas, and he used experimental data from Flettner rotors to estimate the unknown parameters in his equations.

A model for unsteady potential flow in ideal fluids, called the 'Random Walk Source Model' is presented in [8] (see appendix for a brief description). As seen in figure 1, this model generates the shape of a particle front emerging from a line source, creeping towards and past a wing section. The lift coefficient can be predicted by the difference of creeping distance d between the two front segments that have been separated by the wing section and an extended separation line which maintains the Kutta condition. At first sight, the distance seems surprisingly large. However, the result aligns very well with the corresponding lift coefficients that are observed in experiments (see [8]).

The front is a result of a model of unsteady potential flow, and further developments in [9] showed that the trajectory of the mass centre of the particle cloud is deflected as the result of the wing section acting as an obstacle to the particle front. The deflection in the path can be seen as the result of a vertical velocity that is added to the particles while passing the profile. We assume that this vertical velocity is also present in steady flow.

Conservation of momentum implies that the velocity of the air then will have to decrease in the horizontal direction, which in turn must be due to drag forces. In this paper, we apply this property, in addition to parameters satisfying the stability criterion in von Kármán vortex streets, to establish a relation between the drag and lift coefficients. Moreover, when the particles cannot follow the surface of an object, the pressure loss behind the object is derived from the circulation which is naturally generated behind such objects (in viscous fluids). Both approaches intend to improve the understanding of drag of profiles and blunt bodies as a result of the circulation in ideal fluids.

In section 2 we derive a relation between the lift and drag coefficients by considering conservation of momentum of a flow around a wing section in the surrounding fluid in two dimensions. The analogy to a von Kármán vortex street is used to resolve the undetermined parameters. The model is naturally extended to three dimensions by the inclusion of Prandtl's induced drag. We also extend the model by taking into account the pressure conditions behind objects when the fluid particles cannot longer follow the surface of the body. In section 3, the model is validated against published experimental data on wing sections and wings. We also demonstrate the ability of the model to estimate the drag of several types of blunt bodies. Finally, the model is applied to a rotating cylinder, which can be considered as being an example of both a wing section and a blunt body, and the results are very close to the results by Bickley. The results are shown to align well with experimental data.

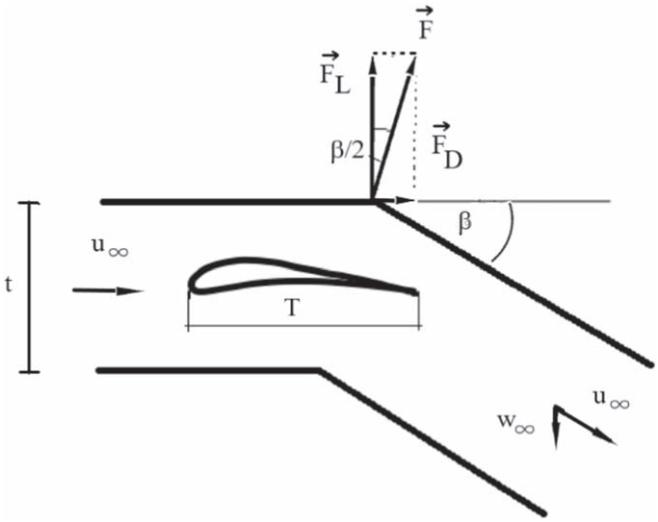

Figure 2. Control volume analysis of a 'particle cloud' passing a wing section. T defines the length of the wing section, b is the depth (into the plane) and $A = b \cdot T$ is the profile area in the horizontal plane. The control volume is representing the particles that are influenced by the geometry of the profile. The height of the control volume is t, and the velocity of the particles is u_∞. The deflection angle of the mass centre trajectory is β.

2. A kinematic model to calculate the drag coefficient

In this section we perform a control volume analysis that leads to equations connecting the ability to generate lift of objects (which is shown in the ability to generate a circulation in a start-stop flow) to the drag of finite and infinite wings and blunt bodies in ideal fluids in a steady flow.

We consider a 'particle cloud' passing a wing section as in figure 2. T defines the length of the wing section, b is the depth (into the plane) and $A = b \cdot T$ is the profile area in the horizontal plane. A control volume is representing the particles that are influenced by the geometry of the profile. The height of the control volume is t, and the velocity of the particles is u_∞. The deflection angle β of the path of the centre of gravity of the particle cloud is seen as the result of a downward pointing velocity component w_∞. The downward pointing velocity is the result of the separation of the fronts during the unsteady flow when the particles pass the wing section. This results in a lack of particles over the profile thus attracting particles from the surroundings. Assuming a density ρ of the fluid, the force **F** acting on the wing section will have a lift component F_L in the vertical direction and a drag component F_D in the horizontal direction.

2.1. Control volume analysis

The speed u_∞ of the particle cloud in figure 2 does not change when passing the wing section. The magnitude of the total force **F** is given by

$$|\mathbf{F}| = 2\rho bt \cdot u_\infty^2 \cdot \sin\frac{\beta}{2}.$$

The component of the force in vertical direction is

$$F_L = 2\rho bt \cdot u_\infty^2 \cdot \sin\frac{\beta}{2} \cdot \cos\frac{\beta}{2} = \rho bt \cdot u_\infty^2 \cdot \sin\beta. \tag{1}$$

The lift force can also be expressed by the lift coefficient, C_L, and substitution of $F_L = C_L \frac{\rho}{2} u_\infty^2 A$ into (1), gives

$$C_L = 2 \cdot \frac{t}{T} \cdot \sin\beta \tag{2a}$$

$$= 2 \cdot \frac{t}{T} \cdot \frac{w_\infty}{u_\infty}. \tag{2b}$$

Here we apply that $A = b \cdot T$ in the first line. That $w_\infty / u_\infty = \sin\beta$ in the second line, is seen from figure 2. Equation (2*a*) relates the lift coefficient of the wing section to the average height, t, of the air volume which is influenced by the wing section, and the direction of the total force of the wing, parameterized by β. We do not know the values of t or β (or equivalently w_∞). In the following we propose an analogy to the von Kármán vortex street to resolve these values.

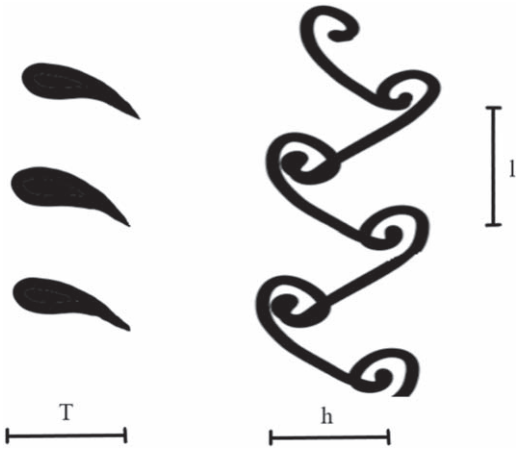

Figure 3. A stack of vertically aligned wing sections in a start-stop sequence generates a von Kármán vortex street. The wing sections are staged according to von Kármán's description and are moved for a short period to generate a circulation, and then removed. Our main assumption is that the vortex centres move with a velocity $w = w_\infty$ downwards, where w_∞ is the downward velocity of the particle cloud in figure 2. We also assume that $T = h$ since the start-stop vortices are centred at the leading and trailing edges of the wing section.

2.2. Von Kármán vortex street—the continuous unfolding of an ideal pair of growing vortices

When a wing section is moved forward and then stopped (for example in a water tank with a free surface), we will see a shedding of a pair of vortices called start-stop vortices. When a plate (which is a wing section with 90° angle of attack) is moved forward in a direction perpendicular to the plate, and then stopped and moved out of the fluid, start-stop vortices will be generated too. The wing section and the plate both have organized fluid in a pair of vortices during the start-stop action. If the plate is moved with constant velocity through the water tank, we will not see a pair of vortices continuously growing during movement, instead we will more likely see a von Kármán vortex street following the plate (depending on the Reynolds number). Now let us make an important assumption, namely that the von Kármán vortex street is one form of the continuous unfolding of the expected growing pair of vortices, carrying the same information about the plate movement that we expect to find in the start-stop vortices after moving the plate out of the fluid. We will show that we can relate w_∞ to the velocity of the vortex centres in a von Kármán vortex street. We assume that start-stop vortices usually unfold as the result of disturbances in the velocity distribution close to the vortices. Depending on the Reynolds number, the unfolding can appear both chaotic, or more regular as in a von Kármán vortex street. We treat both cases as the same macroscopic phenomena.

A wing section moving through a fluid is part of a pair of growing vortices, where the wing section itself is part of the core of one vortex. Now we assume, the pair of growing vortices is unfolding, to a von Kármán vortex street. This leads to assumptions concerning t (the environment of particles which are influenced by the profile) and w_∞.

2.3. Assumptions concerning t and w_∞

The von Kármán vortex street [10, 11], as shown in figure 3, consists of two rows of vortices, each vortex representing a circulation Γ. The ratio between the perpendicular distance h between the two rows of vortices and the distance l between two vortex cores in the same row is given by [11]

$$\frac{h}{l} = \frac{\ln(1+\sqrt{2})}{\pi} \approx 0.280\,5. \tag{3}$$

The vortex centres have a velocity w in the same direction as the moving object. The circulation Γ is related to the velocity w and is given by [11]

$$\Gamma = \sqrt{8}\, w \cdot l = \frac{\pi\sqrt{8}\, wh}{\ln(1+\sqrt{2})}, \tag{4}$$

where l in (3) is substituted in the last equality.

We can make an instantaneous replica of a von Kármán vortex street by constructing a stack of vertically aligned wing sections as shown in figure 3. They are staged according to von Kármán's description in (3) and (4) and are moved for a short period to generate a circulation, and then removed. Our main assumption is that the vortex centres move with a velocity $w = w_\infty$ downwards, where w_∞ is the average downward velocity of the

particle cloud in figure 2. We also assume that $T = h$ since the start-stop vortices are centred at the leading and trailing edges of the wing section.

When the Kutta-condition is applied, the circulation of a wing section is related to the lift coefficient by

$$\Gamma = \frac{1}{2} C_L u_\infty T. \tag{5}$$

Assuming that the circulation of a wing section in (5) equals the circulation of the vortices in a corresponding von Kármán vortex street in (4), with $h = T$ and $w = w_\infty$, we get the following expression for the lift coefficient

$$C_L = \frac{2\pi\sqrt{8}}{\ln(1+\sqrt{2})} \cdot \frac{w_\infty}{u_\infty} \tag{6a}$$

$$= \frac{2\pi\sqrt{8}}{\ln(1+\sqrt{2})} \cdot \sin\beta. \tag{6b}$$

Comparing (2*a*) and (6*b*), the height t of the area that represents the fluid particles that are influenced of the profile geometry, is given by

$$\frac{t}{T} = \frac{\pi\sqrt{8}}{\ln(1+\sqrt{2})} \approx 10.1.$$

This means that the average height of the particle volume influenced by the wing section is approximately 10 times larger than the length of the wing section.

The frequency of vortex shedding is not considered to be of importance here, as the von Kármán vortex street is only *one* representation of a disassembled vortex pair where, in the beginning, one vortex belongs to the wing section and the other belongs to the start vortex. The vortex pair is the result of the wing section attracting particles from the surroundings. *Another* representation of one vortex of the vortex pair is for example the vortices behind a rotating cylinder which usually are seen as turbulent flow. We utilize the assumption that these vortices have not lost the information about the vertical velocity generated by the circulation which is connected to them.

The above results can now be applied to establish a relation between the drag coefficient and the lift coefficient.

2.4. Model—fluid particles following the surface of an object

We can now relate the drag and the lift coefficients for objects where the fluid particles follow the surface of an object, based on the von Kármán vortex street analogy. From figure 2, the horizontal drag force component of the force is given by

$$F_D = F_L \tan\frac{\beta}{2} = F_L \frac{\sin\beta}{2\cos^2\frac{\beta}{2}} \approx F_L \frac{\sin\beta}{2},$$

where the approximation is valid for small β. The same relation is valid for the drag and lift coefficients:

$$C_D \approx C_L \frac{\sin\beta}{2} = \left(\frac{C_L}{2\pi}\right)^2 \frac{\pi \ln(1+\sqrt{2})}{\sqrt{8}}, \tag{7}$$

where the expression for $\sin\beta$ in (6*b*) is used in the last line.

Equation (7) connects the lift coefficient of a wing section to the drag coefficient in a friction-less fluid in a 2-dimensional model, and defines induced drag in two dimensions. For finite wings in three dimensions with aspect ratio $\Lambda = b/T$, we include the contribution from Prandtl's induced drag and get

$$C_{D,\Lambda} = \left(\frac{C_{L,\Lambda}}{2\pi}\right)^2 \frac{\pi \ln(1+\sqrt{2})}{\sqrt{8}} + \frac{C_{L,\Lambda}^2}{\pi\Lambda}. \tag{8}$$

Here $C_{D,\Lambda}$ and $C_{L,\Lambda}$ are the respective drag and lift coefficients of a 3-dimensional wing in ideal fluid. For $\Lambda = 1$, Prandtl's induced drag represents 93% of the total drag in (8). However, for larger aspects ratios, the first term becomes more dominant, and for $\Lambda = 13$ the two terms are of equal size.

2.5. Extended model—when fluid particles do not follow the surface of an object

Following the idea that the drag in ideal fluids is the result of the ability to produce lift (or a circulation), we have a look at the wing section in figure 4(b). Here we show a profile where a part of the trailing edge is cut off. The result is a vertical step in the contour of the profile. How will this step influence the drag? Let us imagine that we make this cut closer and closer to the profile nose. At the end we will get a kind of flat plate at 90° angle of attack.

As we know, a plate does not produce lift when perpendicular to the flow. Equation (7) does not answer the question about the value of the drag coefficient in this case, there is something missing. We know, a plate at a

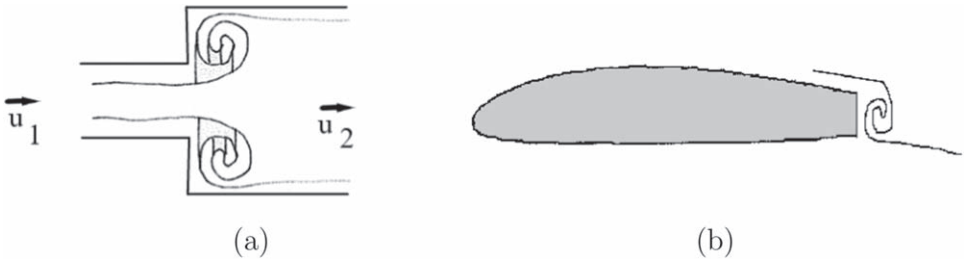

Figure 4. Analogy between (a) a sudden expansion in a pipe and (b) a profile with step (blunt body). The velocity of the fluid in the small diameter pipe is transferred to the vertical wall between the two pipe sections and the pressure loss is $\Delta P = \rho/2 \cdot (u_1 - u_2)^2$. u_1 is the velocity in the small diameter pipe, and u_2 the velocity in the wider pipe after the sudden expansion.

small angle of attack is like a wing section, one vortex is caught by the wing, the other, the start vortex, is shed. At higher angle of attack, the caught vortex transfers velocity to the back of the plate. This phenomenon shall be seen here to be similar to the Carnot pressure loss, as in figure 4(a) where a flow in a small pipe experiences a sudden expansion into a larger pipe. The pressure loss is $\Delta P = \rho/2 \cdot (u_1 - u_2)^2$, where u_1 is the velocity in the small diameter, and u_2 the velocity in the wider diameter after the sudden expansion. Moreover, the velocity of the fluid in the small diameter pipe is transferred to the vertical wall between the two pipes.

Let u_Γ be the velocity at the trailing edge of a wing profile when we replace the profile with a vortex to maintain the Kutta condition. In the same way as u_1 in the expanding pipe in figure 4(a) is transferred to the vertical walls, the velocity u_Γ in figure 4(b) is transferred in a vortex movement to the backside of the profile.

In a similar way, while the submitted pressure in figure 4(a) is derived from the velocity difference $u_1 - u_2$, we suggest that the submitted pressure in figure 4(b) is given by u_Γ, such that the reduced pressure behind the profile is

$$\Delta P = \frac{\rho}{2} u_\Gamma^2. \tag{9}$$

More generally, we suggest that the trailing edge velocity u_Γ of a blunt body results from its ability to produce a circulation.

Let us call the force on the profile as the result of the reduced pressure behind the blunt body a Carnot force. Using ΔP in (9), the Carnot force is given by

$$F_{D,Carnot} = \Delta P \cdot A_\perp = \frac{\rho}{2} u_\Gamma^2 \cdot T_\perp b. \tag{10}$$

$A_\perp = T_\perp b$ is here the projection area of the profile perpendicular to the direction of u_∞, $T_\perp$ is the height of the profile perpendicular to the flow direction, and b is the width of the profile into the plane. The corresponding contribution to the drag coefficient of a 2-dimensional profile from the force $F_{D,Carnot}$ in (10) is then given by

$$C_{D,Carnot} = \frac{2F_{D,Carnot}}{\rho u_\infty^2 T b} = \frac{u_\Gamma^2}{u_\infty^2} \cdot \frac{T_\perp}{T}, \tag{11}$$

where T is defined to be the length along the longest dimension of the object.

The drag C_D in (7), which accompanies the lift C_L of a profile, has to be extended to include this blunt body drag, when we assume that the flow particles cannot follow the contour of an object (some seconds) after the object has been accelerated to a constant velocity u_∞. Extending the expression for the drag coefficient C_D in (7), we include $C_{D,Carnot}$ in (11) and write

$$C_D = \left(\frac{u_\Gamma}{u_\infty}\right)^2 \frac{\pi \ln(1+\sqrt{2})}{\sqrt{8}} + \left(\frac{u_\Gamma}{u_\infty}\right)^2 \frac{T_\perp}{T} \tag{12a}$$

$$= \left(\frac{C_L}{2\pi}\right)^2 \frac{\pi \ln(1+\sqrt{2})}{\sqrt{8}} + \left(\frac{C_L}{2\pi}\right)^2 \frac{T_\perp}{T}, \tag{12b}$$

where we use that the lift coefficient of a wing section can be expressed in terms of the velocity of circulation u_Γ at the trailing edge when the Kutta-condition is applied: $C_L = 2\pi u_\Gamma / u_\infty$.

Equation (12*a*) connects the ability of a blunt body to maintain a circulation (or generate circulation in a viscous fluid) to the drag in ideal fluids. In a start phase, the fluid particles will follow the contour of a wing section or a blunt body, but after a short time, the particles do not longer follow the contour, but they transfer the velocity u_Γ in a vortex movement to the backside of the body.

A circulation is not necessarily resulting in lift. Since C_L, as it is used when substituting u_Γ/u_∞ in (12*a*), represents the ability of a body to maintain a circulation (characterized by u_Γ), this means that for bodies without

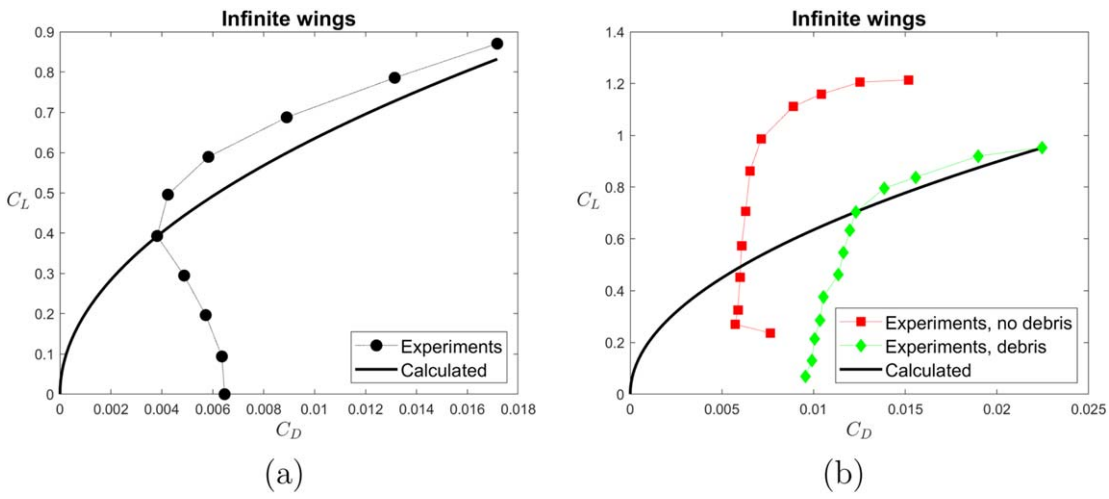

Figure 5. Comparison of the predicted drag coefficient (for ideal fluid) with experimental data corresponding to an infinite wing. (a) Data reproduced from [12] with Re $=$ 1 020 000. (b) Data reproduced from [13] with Re $=$ 1 500 000. The nose geometry of the wing profile is such that a separation bubble is expected. This effect is reduced when debris is applied. (a), (b) Model prediction (solid curves), calculated with (7): $C_D = \left(\frac{C_L}{2\pi}\right)^2 \frac{\pi \ln(1+\sqrt{2})}{\sqrt{8}}$.

lift, we can define a *theoretical lift coefficient*, defined by $C_L \equiv 2\pi u_\Gamma / u_\infty$. The direction of the circulation generated by a symmetrical blunt body cannot be determined. However, we can assume that it is not constant but alternating in different directions with a frequency depending on the Reynolds number. Each circulation can generate a lift, but the alternating directions compensate each other and result in zero lift. This means that behind a blunt body the separation line is not in a constant position, but is jumping or moving up and down close to the rear edge. If C_L is known, (12*b*) can be used to calculate the drag. In section 3.2 we will demonstrate how the theoretical C_L and u_Γ / u_∞ can be estimated when there is no lift.

Notice that for blunt bodies in three dimensions with finite aspect ratio $\Lambda = b/T$, (12*b*) can also be extended to include the contribution from Prandtl's induced drag. However, such settings are not explored further in this paper.

3. Validation of model against experimental results

The novel and simple theoretical connection between drag and lift coefficients presented in section 2 differs fundamentally from those methods commonly in use. We have not performed experiments to validate the model, but in this section we demonstrate how the model performs on already published experimental data. This is done both for profiles where the fluid particles are assumed to follow the contour of the body (section 3.1) and for blunt bodies where a detachment is expected (section 3.2). Notice that there are no free parameters that must be estimated to establish the relation. However, when there is no lift, the theoretical lift coefficient needs to be determined in order to obtain a value for the drag coefficient. Finally, in section 3.3, we compare published experimental data of rotating cylinders to the predictions from our model and to the results of Bickley.

3.1. Validation of model—fluid particles following the surface of an object

To test the assumptions in section 2.4, we have compared experimental data with the calculated drag using (7) and (8). These are shown in figures 5 and 6, respectively.

3.1.1. Infinite wings

In figure 5(a), we see an example where the predicted drag coefficients correspond well with experimental data for experiments with high Reynolds number (Re $=$ 1 020 000). The deviations of the drag C_D for small values of C_L is expected as the contribution from surface effects becomes dominant. The lift coefficient exceeds the predicted values in connection with higher Reynolds numbers, which can be the effect of fluid particles not following the expected pattern on the surface of the profile.

Figure 5(b), shows experimental data for two similar wing sections with a geometry where a separation bubble can be expected. One wing section is without debris, the other wing section is with debris. The profile without debris is expected to have a separation bubble close to the nose adding lift and reducing drag. With

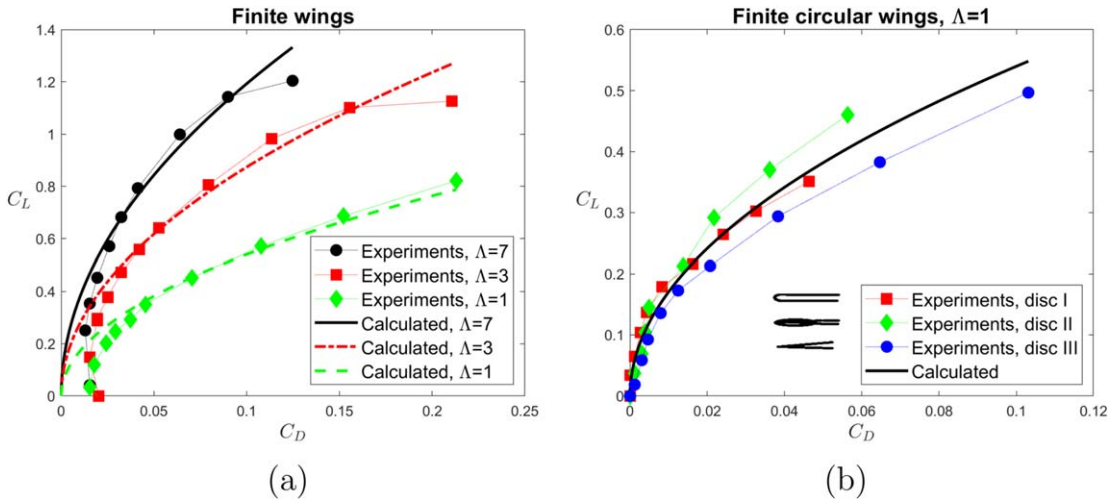

Figure 6. Comparison of the predicted drag coefficient (for ideal fluid) with experimental data for finite wings. Measured lift and drag coefficients for finite aspect ratios reproduced from [14]. (a) Three wings with aspect ratios Λ ranging from 1 to 7 (aspect ratios given in the figure). (b) Circular wings with aspect ratio $\Lambda = 1$ and different nose geometries (indicated in figure). The drag force component F_D for $C_L = 0$ is subtracted from these data sets. (a), (b) Model prediction calculated with (8): $C_{D,\Lambda} = \left(\frac{C_{L,\Lambda}}{2\pi}\right)^2 \frac{\pi \ln(1+\sqrt{2})}{\sqrt{8}} + \frac{C_{L,\Lambda}^2}{\pi\Lambda}$.

debris on the nose the turbulent boundary layer is reducing the bubble effect. The debris brings the data closer to our model. Notice that our model is not yet extended to take the effect of separation bubbles into account.

3.1.2. Finite wings

In figure 6(a), the model in (8) exhibits good correspondence with experimental data from finite wings. For $\Lambda = 1$ and $\Lambda = 7$, the drag due to the first term in our model explains 7% and 35% of the total drag, respectively. The remaining part of the drag is due to Prandtl's induced drag. As expected, for high values of C_L, the data deviates from the model due to stalling.

In figure 6(b) we see that experimental data suggest that the drag is higher for wing geometries where a separation bubble is considered less likely to appear as a result of the nose geometry (discs I and III). Our model predicts 8% more drag than Prandtl's induced drag (with aspect ratio $\Lambda = 1$) and is closer to the observed results for discs I and III.

3.2. Validation of extended model—when fluid particles do not follow the surface of an object

To test the assumptions in section 2.5, we have compared experimental data with the calculated drag using (12*b*). These are shown in figures 7 and 8.

3.2.1. Drag of a plate of infinite span at 90° angle of attack

Following [8], the lift coefficient of a wing section can be expressed in terms of the distance d between the separated particle fronts at the separation line behind the wing section in an unsteady potential flow as shown in figure 1,

$$C_L = 2\pi\frac{d}{T}. \tag{13}$$

For a plate perpendicular to the flow direction, it can be argued that the distance d equals the distance from the top edge of the plate to the separation line at the bottom edge of the plate, such that $d = T_\perp$. According to (13), we then obtain a theoretical lift coefficient of $C_L = 2\pi$ for a plate (i.e. its ability to generate a circulation). For such plates (including the extended plates presented below), (12*b*) now takes the form

$$C_{D,90°plate} = \left(\frac{2\pi}{2\pi}\right)^2 \frac{\pi\ln(1+\sqrt{2})}{\sqrt{8}} + \left(\frac{2\pi}{2\pi}\right)^2 \frac{T_\perp}{T} = \frac{\pi\ln(1+\sqrt{2})}{\sqrt{8}} + \frac{T_\perp}{T}. \tag{14}$$

For a thin plate, $T_\perp = T$, and we write

$$C_{D,90°plate} = \frac{\pi\ln(1+\sqrt{2})}{\sqrt{8}} + 1 = 1.98.$$

This is close to the published result in [12] for Re > 10000, where $C_{D,90°plate} = 2.1$.

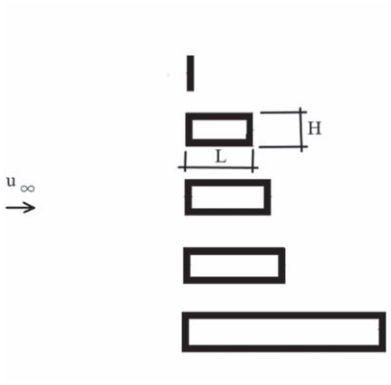

	published drag	calculated drag
H/L= $T_\perp$/T= 1	2.1	1.97
H/L= $T_\perp$/T= 0.5	1.8	1.48
H/L= $T_\perp$/T= 0.4	1.4	1.37
H/L= $T_\perp$/T= 0.33	1.3	1.31
H/L= $T_\perp$/T= 0.16	0.9	1.14

Figure 7. Comparison of the predicted drag, C_D, of an extended plate of infinite span (friction-less fluid), to experimental data taken from [12]. Model prediction using $C_L = 2\pi$ in (14): $C_{D,90°plate} = \frac{\pi \ln(1+\sqrt{2})}{\sqrt{8}} + \frac{T_\perp}{T}$.

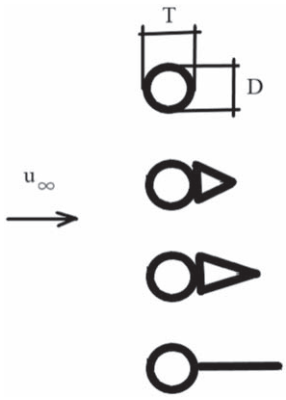

	diameter length ratio	published drag	calculated drag
	D/T=1	Cd=1.2	(Cd=1.2)
	D/T=0.5	Cd=0.88	Cd=0.895
	D/T=0.4	Cd=0.80	Cd=0.83
	D/T=0.33	Cd=0.84	Cd=0.79

Figure 8. Comparison of the predicted drag coefficient (in ideal fluid) with experimental data for infinite cylinders with added objects. Measured lift and drag coefficients reproduced from [12]. Model prediction is calculated with (12*b*), where $T_\perp = D$, and $C_L = 4.89$ (estimated based on experimental data for an infinite cylinder): $C_D = \left(\frac{C_L}{2\pi}\right)^2 \frac{\pi \ln(1+\sqrt{2})}{\sqrt{8}} + \left(\frac{C_L}{2\pi}\right)^2 \frac{T_\perp}{T}$.

Extended plates differ in a ratio $T_\perp/T$. Equation (14) takes this into account and is compared to experimental values in figure 7. For all objects, T is defined to be the length along the longest dimension of the object.

3.2.2. Drag of a cylinder of infinite span with added objects

We now turn to the estimation of the drag coefficient of an infinite cylinder with added objects. Since we cannot determine the point of detachment of the boundary layer, the theoretical lift coefficient, C_L, must be inferred by experimental data.

The experimentally determined drag coefficient of an infinite cylinder (i.e. cylinder with discs) is given by $C_{D,cylinder} = 1.2$ (valid for $\mathrm{Re} = 16000 - 180000$, [12, 15]). By rearranging (12*b*) and using the experimental value of $C_{D,cylinder}$, we can infer the value of the theoretical lift coefficient (here meaning the theoretical ability to produce lift) of an infinite cylinder:

$$C_{L,Cylinder} = 2\pi \sqrt{\frac{C_{D,Cylinder}}{\frac{\pi \ln(1+\sqrt{2})}{\sqrt{8}} + \frac{T_\perp}{T}}} = 2\pi \sqrt{\frac{1.2}{\frac{\pi \ln(1+\sqrt{2})}{\sqrt{8}} + \frac{1}{1}}} = 4.89, \tag{15}$$

where we use that $T = T_\perp$ for a cylinder in the last equality.

In figure 8, this value, $C_L = C_{L,Cylinder} = 4.89$, is used as input value in (12*b*) to calculate the drag coefficients for the combinations of an infinite cylinder with added objects where the ratio $T_\perp/T$ varies. Again, the model gives estimates reasonably close to experimental values.

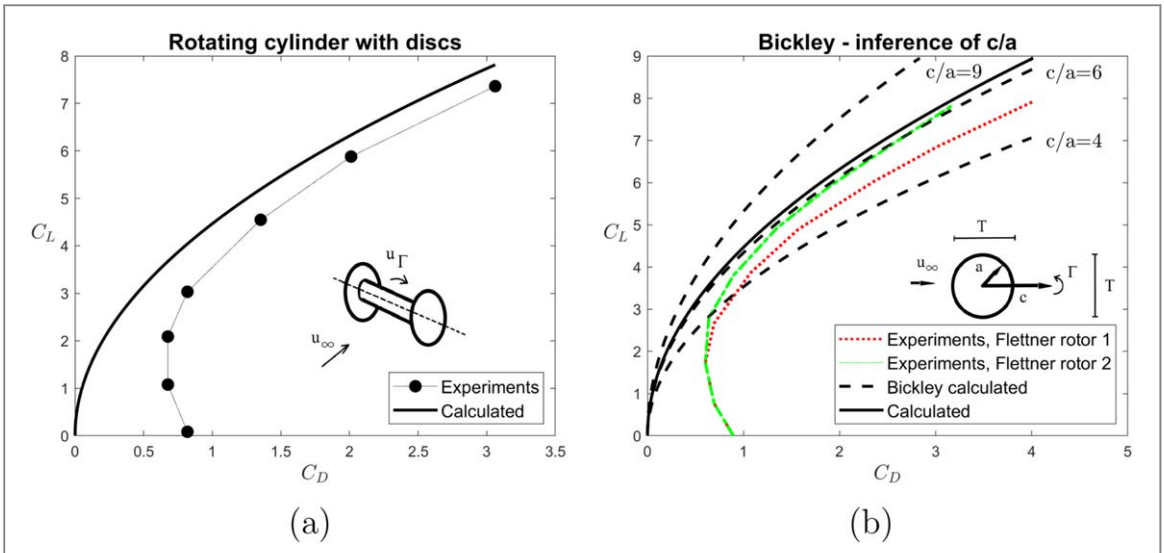

Figure 9. Comparison of the predicted drag coefficient (in ideal fluid) with experimental data for rotating cylinders in 2-dimensional flow. (a) Data from rotating cylinders with end discs reproduced from [12]. (b) Flettner rotor data reproduced from [7]. In Bickley's model an outside vortex with same circulation as the rotating cylinder with radius a, is placed at various positions c behind the cylinder. The resulting drag is given by (18): $C_D = \frac{C_L^2}{4\pi} \cdot \frac{a}{c} \cdot 4/\left(1 - \frac{a^4}{c^4}\right)^2$. Bickley found that $c/a = 6$ gave the best model fit to the experimental data. (a), (b) The solid curves show the predicted drag suggested in this paper, calculated with (12*b*): $C_D = \frac{C_L^2}{4\pi}\left(\frac{\ln(1+\sqrt{2})}{\sqrt{8}} + \frac{1}{\pi}\right)$, where $T_\perp/T = 1$.

3.3. Drag of a rotating cylinder with infinite span

If it is possible to calculate the drag of a static cylinder by defining an ability to produce lift, which leads to drag, it should be possible to calculate the drag coefficient of a rotating cylinder of infinite span using the published values of the lift coefficient, which is heavily influenced by the rotation. This is done in figure 9(a). Calculated values show good agreement with measured data of a rotating cylinder between limiting discs. Bickley [7] examined the case of a two-dimensional flow past a rotating circular cylinder, investigating the resulting force on the cylinder by using the full pressure equation, and then taking the velocity potential out of the stream function. Behind the cylinder, he placed a vortex with the same circulation as the cylinder. As a result, he got two formulas defining the drag and lift coefficients containing the circulation Γ, the velocity of the flow against the cylinder u_∞ and a relation between cylinder diameter a and the distance c between the centre of the cylinder and the outside vortex core [7]:

$$C_D = \frac{1}{4\pi} \cdot \frac{a}{c} \cdot \left(\frac{\Gamma}{a u_\infty}\right)^2, \tag{16}$$

$$C_L = \frac{1}{2}\left(1 - \frac{a^4}{c^4}\right) \cdot \frac{\Gamma}{a u_\infty}. \tag{17}$$

Combining (16) and (17) gives

$$C_D = \frac{C_L^2}{4\pi} \cdot \frac{a}{c} \cdot \frac{4}{\left(1 - \frac{a^4}{c^4}\right)^2} = \frac{C_L^2}{4\pi} \cdot 0.667\,7\ldots, \tag{18}$$

where $c/a = 6$ is used in the last equality, as this gave best model fit to Bickley's experimental data. Bickley also experimented with different vertical positions of the outside vortex behind the cylinder, but found that the outside vortex centre should be placed in the same vertical position as the centre of the cylinder in order to obtain best fit to the experimental data. Equation (18) agrees very well with our suggested solution in (12*b*) where we set $T = T_\perp$, such that

$$C_D = \frac{C_L^2}{4\pi}\left(\frac{\ln(1+\sqrt{2})}{\sqrt{8}} + \frac{1}{\pi}\right) = \frac{C_L^2}{4\pi} \cdot 0,\ 6299\ldots$$

In figure 9(b), the results from Bickley and the experimental data for the Flettner rotors (which he published without references, but which are very similar to the data in figure 9(a) from [12]) are compared to our results.

4. Discussion

Based on a random walk source model where particles have no viscosity, we observe that a particle front moving towards a profile in a simulated unsteady flow (particles are coming out of a line source, pushing each other towards the profile), will be separated at the profile into two fronts. One front passing the upper part of the profile, one passing the lower part of the profile. Keeping these two fronts separated at the rear edge of the profile with a separation line parallel to the flow velocity (to maintain the Kutta condition), we see a geometrical representation of a potential difference which leads, together with the flow velocity, to the circulation of the profile. This circulation is defining the theoretical lift coefficient the profile geometry can generate. We have in this model the unusual view of a geometrical representation of a potential difference, generated by the wing geometry making a 'gap in the area' close to the wing section. This gap is in reality attracting particles from the surroundings, and results in a circulation.

The same effect is known in connection with start-stop vortices generated by wing sections that have been accelerated and stopped. They generate in 2D a pair of vortices moving downwards (see figure 3). The vortices are a result of attracted particles that have to continue the movement as a result of inertia. We demonstrate that the physical properties of the vortex pair can be used to define the relation between the drag and lift coefficients of a wing section in two dimensions.

Observations from the Random Walk Source Model showed a deflection of the path of the mass centre of the particle cloud (see figure 1) passing the wing section (or other objects). A wing section is constantly attracting particles from the surroundings and thus generating a downwash velocity w_∞.

In this paper the assumption is made, that information concerning the influenced volume and downstream or lateral velocity generated from a wing section or other objects can be found in the ability of an object to generate a vortex pair in a start sequence. This vortex pair can unfold into a von Kármán vortex street under known conditions. Using the parameters of a von Kármán vortex street leads to the induced drag in two dimensions of infinite wing sections in ideal fluids, assuming the lift is known (see (7)):

$$C_D = \left(\frac{C_L}{2\pi}\right)^2 \frac{\pi \ln(1+\sqrt{2})}{\sqrt{8}}.$$

For finite wings with aspect ratio Λ, we include Prandtl's induced drag in three dimensions such that (see (8))

$$C_{D,\Lambda} = \left(\frac{C_{L,\Lambda}}{2\pi}\right)^2 \frac{\pi \ln(1+\sqrt{2})}{\sqrt{8}} + \frac{C_{L,\Lambda}^2}{\pi\Lambda}.$$

For 2-dimensional blunt bodies, where we expect that the fluid particles cannot follow the contour, we take the pressure reduction behind the object into account and write (see (12*b*))

$$C_D = \left(\frac{C_L}{2\pi}\right)^2 \frac{\pi \ln(1+\sqrt{2})}{\sqrt{8}} + \left(\frac{C_L}{2\pi}\right)^2 \frac{T_\perp}{T}.$$

This equation for blunt bodies contains an additional part, which takes into account the effect of the vortex transferring the velocity u_Γ to the back of the body. In this case, this means an increase of drag. Of course, for finite blunt bodies in 3D, the equation could also be extended to include Prandtl's induced drag.

The model assumptions was tested by comparing published polar curves of wing sections and drag coefficients of blunt bodies with the respective calculated data. The agreement of the drag of wing sections shows a close resemblance for higher values of lift. For smaller values of lift coefficients our model differ from experimental data, which is expected, as the friction effects in the real fluids is the dominating cause of the drag.

We also show that it is possible to calculate the drag coefficient of a rotating cylinder of infinite span. Calculated values show good agreement with measured data of a rotating cylinder between limiting disks. The presented equations suggest a physical parameter, which replace a parameter that was empirically estimated by W. G. Bickley from experimental data of rotating cylinders.

Further experimental validations of our models would be valuable. In airfoil design the trailing edge of real wings cannot be made as pointed as desired to fulfil the Kutta condition. Accordingly, an airfoil is to some degree a blunt body, much in the same way as a rotating cylinder. It would therefore be of particular interest to experimentally determine how the drag increases when the trailing edge of a wing section is cut off vertically closer and closer to the leading edge (see figure 4(b)).

Depending on the geometry of wing sections we can observe that lift and drag can differ from the expected values, perhaps due to a generated pressure distribution close to the nose where particles are not able to follow the geometry. This distribution seems to be able to generate less or more lift and less or more drag due to the orientation of the geometry part where the particles leave the surface. It has been observed, that profile data where lift is underestimated in our model and drag is overestimated, comes closer to our estimated two dimensional induced drag when debris on the nose influences the flow close to the nose. Such effects will be part of further research.

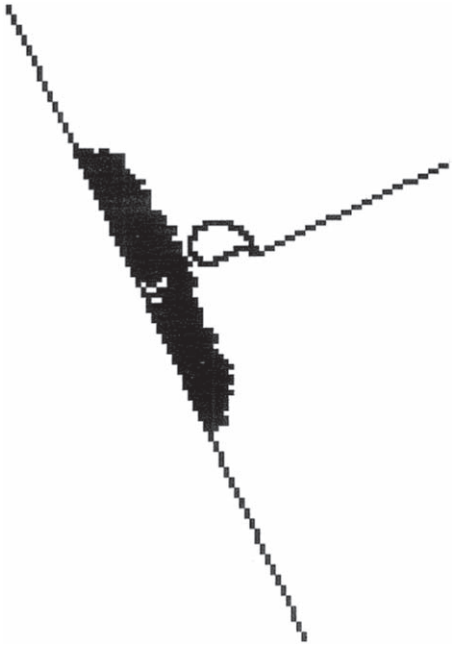

Figure A1. Fluid flow in the form of a particle cloud moving towards a wing section.

Appendix. Random walk source model

This appendix contains a brief summary of the Random Walk Source Model [8]. Fluid flow in the form of a particle cloud moving towards and past obstacles is modelled on a 2-dimensional orthogonal lattice with coordinates (i, j) as shown in figure A1. Each cell in the lattice can take three different values:

- $a_{i,j} = 0$, cell is not yet occupied,
- $a_{i,j} = 1$, cell is already occupied by a particle,
- $a_{i,j} = 2$, cell cannot become occupied (boundary cell).

From the start certain cells along one of the boundaries are defined as source cells and are assigned the value $a_{i,j} = 1$, but none of the other cells are occupied by a particle. At the first time step, one particle is released from a random source cell (singularity of the source). This means that one particle has left the centre of the source. Of the four neighbouring cells the particle moves to a randomly selected cell (i, j) and proceeds according to the value of this cell:

- Cell is empty ($a_{i,j} = 0$): The particle can settle down at this cell (i, j), and the cell changes value to $a_{i,j} = 1$.
- Cell is occupied ($a_{i,j} = 1$): The particle proceeds to another randomly selected neighbouring cell in orthogonal direction from (i, j).
- Cell is at the boundary ($a_{i,j} = 2$): The particle returns to the previous cell and choose randomly one of the other three neighbouring cells.

This random walk process continues until the particle settles down at an empty cell. Then the algorithm starts over again by releasing a new particle from a random source cell.

The simulation can be viewed as the behaviour of a fluid particle, coming out of a source, and making a random walk to the front of the region occupied by particles. This region is built from all particles that have previously left the source. The particles bounce off the obstacles in the flow region, and eventually settle down in the first free space at the particle front.

We have generated a particle displacement model. A physical particle coming out of a source will displace particles that have already left the source. However, in this model a particle coming out of the source 'steps on the heads' of other particles and settles down as one particle that has been displaced by the particle coming out of

the source. In this way the identities of the particles are exchanged. The boundary is thus viewed as an equipotential line of unsteady potential fluid flow.

To simulate a parallel flow approaching a wing profile, we situate the source cells as described above on a line which stands perpendicular to the flow direction in front of the wing section. Ideally, one should choose a start distance where we assume the average particle path is not influenced by the profile. The greater the distance the better. However, since calculation time increases rapidly with increasing distance, we have typically used a distance that was one wing section length from the nose of the profile in simulations.

The boundary cells with the value $a_{i,j} = 2$ define the contour of the examined wing sections. The separation line at the trailing edge also consists of cells that are set to the value $a_{i,j} = 2$, in order to keep the fronts separated (according to the Joukowsky rule).

ORCID iDs

R W Meyer https://orcid.org/0000-0003-1249-7264
S Erland https://orcid.org/0000-0003-0175-8801

References

[1] Lanchester F W 1908 Aerodonetics: constituting the second volume of a complete work on aerial flight *Aerial Flight* 2 (London: Constable & Co. Ltd.)
[2] Prandtl L 1918 Tragflügeltheorie: I. Mitteilung *Göttinger Nachr.* **1918** 451–77
[3] Schlichting H and Gersten K 2017 *Boundary-Layer Theory* (Berlin, Heidelberg: Springer) (https://doi.org/10.1007/978-3-662-52919-5)
[4] Eppler R 1990 *Airfoil Design and Data* (Berlin, Heidelberg: Springer) (https://doi.org/10.1007/978-3-662-02646-5)
[5] Drela M 1989 Xfoil: an analysis and design system for low reynolds number airfoils *Low Reynolds Number Aerodynamics* (*Lecture Notes in Engineering* vol 54) ed) ed T J Mueller (Berlin, Heidelberg: Springer) pp 1–12
[6] Saffman P G 1993 Vortex Dynamics *Cambridge Monographs on Mechanics* (Cambridge: Cambridge University Press) (https://doi.org/10.1017/CBO9780511624063)
[7] Bickley W G 1928 The influence of vortices upon the resistance experienced by solids moving through a liquid *Proc. R. Soc. Lond. A Math. Phys. Sci.* **119** 146–56
[8] Meyer R 1997 Random walks and hydrodynamical lift from wing sections *Physica* A **242** 230–8
[9] Meyer R 2001 Random walk source model and lift coefficent *Technical Soaring* **25** 167–72
[10] von Kármán T 1911 Ueber den mechanismus des widerstandes, den ein bewegter körper in einer flüssigkeit erfährt *Göttinger Nachr.* **1911** 509–17
[11] von Kármán T 2013 On the mechanism of the drag a moving body experiences in a fluid *Prog. Aerosp. Sci.* **59** 16–9 Special issue: Theodore von Kármán
[12] Eck B 1966 Strömungstechnische Messungen *Technische Strömungslehre* (Berlin, Heidelberg: Springer) pp 418–458
[13] Wurz W 1997 Polarenmessungen an den profilen ww97-155 und ww97-142 *Institutsbericht des IAG* (Universität Stuttgart)
[14] Schlichting H and Truckenbrodt E 2001 Tragflügel endlicher Spannweite bei inkompressibler Strömung *Aerodynamik des Flugzeuges* (Berlin, Heidelberg: Springer) pp 1–132
[15] Tietjens O G and Prandtl L 1957 *Applied Hydro- and Aeromechanics: Based On Lectures of L. Prandtl* (*Engineering Societies Monographs*) (New York: Dover Publications, inc.)